

# Geant4 Simulations for Diagnostic Elements in the FLASH Dump Line

Andriy Ushakov and Sabine Riemann

*Deutsches Elektronen-Synchrotron, Platanenallee 6, 15738 Zeuthen, Germany*

## Abstract

Diagnostic elements as halo monitors and long ionization chambers were installed in the FLASH dump line to monitor the beam position and to ensure that the beam impinges the central part of the absorber entrance. Simulations were performed to determine the number of particles passing the diagnostic elements and their energy in case of misdirected beams and beam losses. In this note the results are presented, they are useful to interpret the sensor signals.

## 1 Introduction

To avoid losses of the electron beam in the FLASH dump line, the beam position is monitored upstream the dump. Directly in front of the dump, between exit window and dump surface, diamond and sapphire sensors are installed. These sensors detect particles in the beam halo and allow to indicate a significant misdirection of the beam. A similar configuration of diamond sensors is also used for beam condition monitoring at the CMS experiment. To fully understand and interpret the signals measured with diamond and sapphire sensors in the FLASH dump line, simulations of the beam passing the exit window are needed. The sensors detect particles from the beam halo but also particles from scattering and Bremsstrahlung processes in the exit window and the dump. Along the beamline between sweeper and exit window, four ionization chambers made of air-filled coax-cables are installed. They are sensitive to particle losses and used to monitor to some extent the beam position in the dump beam line.

In our studies a 1-GeV electron beam was considered. Different beam paths between sweeper and dump were simulated. The distributions and spectra of particles hitting the sensors or passing the ionization chambers were determined. The simulation was performed using Geant4 [1].

## 2 The Model

The FLASH beam dump line is schematically shown in Fig. 1. The last part of this vacuum section was modified in 2009. In the new design the beam position monitor (BPM15) is located outside the concrete shielding block and placed close to the sweeper. The detailed views of vacuum beam pipe end, exit window, detector holder, diamond/sapphire sensors and bellow are shown in Fig. 2. The bellow is directly connected to the dump. The parts of the beam dump and their dimensions are shown schematically in Fig. 3.

The main parts of the FLASH beam dump area such as dump vacuum beam pipe, exit window, sensors, sensor holder, bellow, dump and concrete shielding were modeled using Geant4. The general view of this model is shown in Fig. 4. In addition to the geometrical model, some particle tracks are shown in this figure. The elevation angle between the vacuum pipe axis and ground (floor) plane was kept, the beam pipe axis was selected as z-axis in Geant4 model.

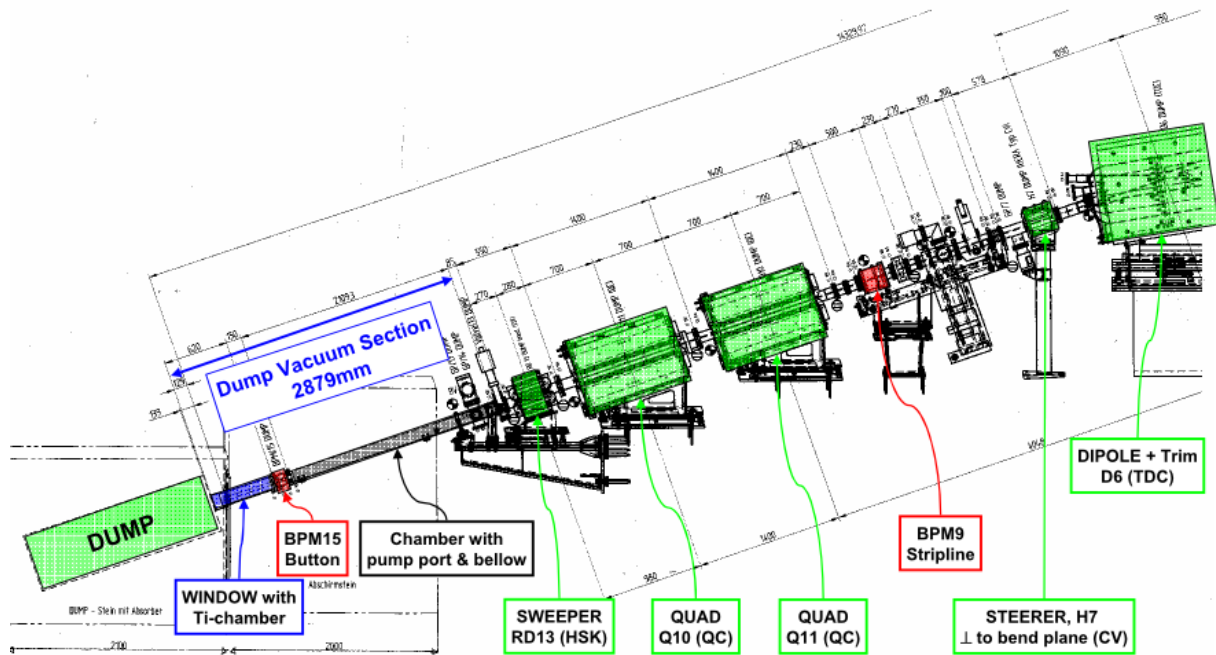


Figure 1: FLASH beam dump line.

An enlarged view of the region between exit window and beam dump is shown in Fig. 5 and 6. In Fig. 5 only the pure sensors are shown. To protect the sensors they are surrounded by copper cups as indicated in Fig. 2. The exit window is made of titanium and 0.5 mm thick. Two graphite disks are placed on both sides of the exit window, their centric thickness is 10 mm.

## 2.1 Sensors

The four diamond and four sapphire sensors are located between exit window and beam dump. The thickness of the 12×12-mm diamond sensors is 0.3 mm, the density is 3.52 g/cm<sup>3</sup>. The thickness of the 10×10-mm sapphire sensors is 0.5 mm; the density of sapphire (Al<sub>2</sub>O<sub>3</sub>) is 3.98 g/cm<sup>3</sup>. The distance between center of sensors and beam pipe axis is 55 mm. For reasons of symmetry in the Geant4 model, all sensors were rotated by 22.5°, so that the vertical (y,z)-plane runs between the two top and the two bottom sensors (see Fig. 6).

In order to monitor the beam position in the simulations, a thin virtual sensor disk was added close to the real sensor plane.

## 2.2 Ionization chambers

Four ionization chambers (IC) are placed around the titanium beam pipe, between sweeper and graphite disk of the exit window (see Fig. 5). The IC are modelled as tubes of approximately 3.3 m length and 12.7 mm diameter. The space between outer surface of the beam pipe and IC is 1 mm. The tube material consists of a thin copper layer filled with air.

## 3 Simulation procedure

The simulations with Geant4 assumed a mono-energetic beam of 1 GeV. Two options were considered: a pencil-like beam and a beam with a Gaussian profile. In all simulations the

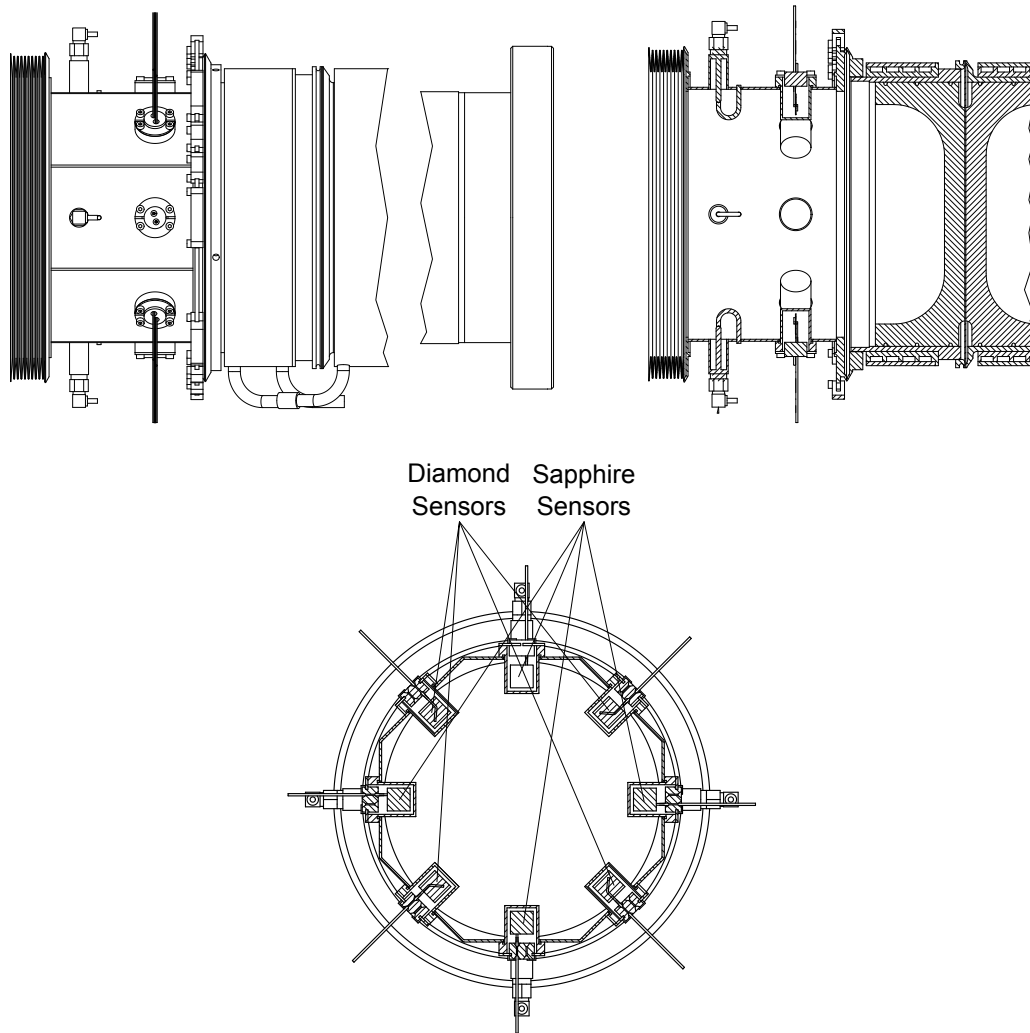


Figure 2: Drawings of beam pipe end, exit window, sensors and bellow: view without cut (top-left), with vertical cut (top-right) or with transverse cut (bottom).

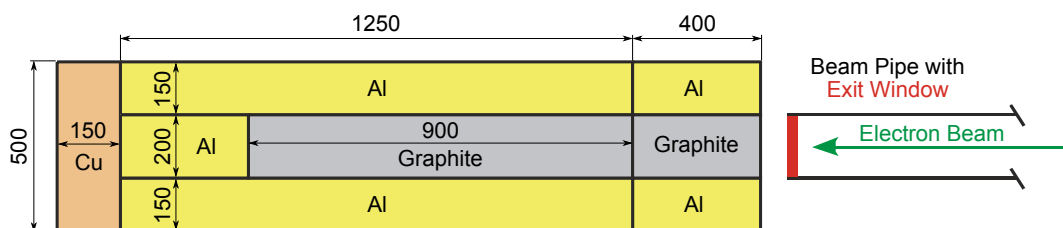


Figure 3: Sketch of FLASH beam dump.

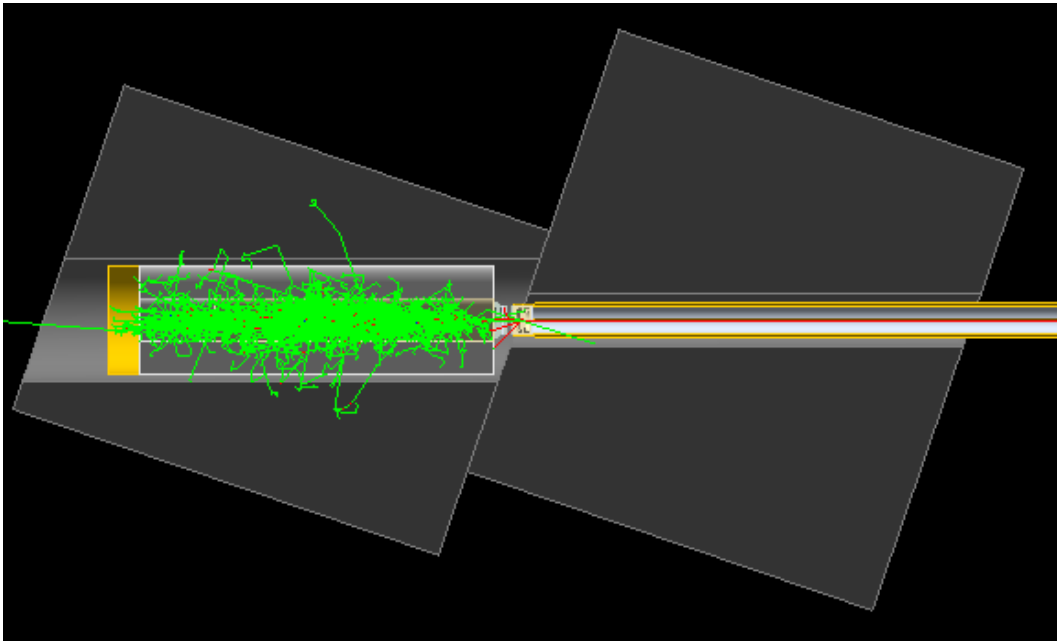


Figure 4: Geant4 model with few simulated particle trajectories of electrons (red) and photons (green).

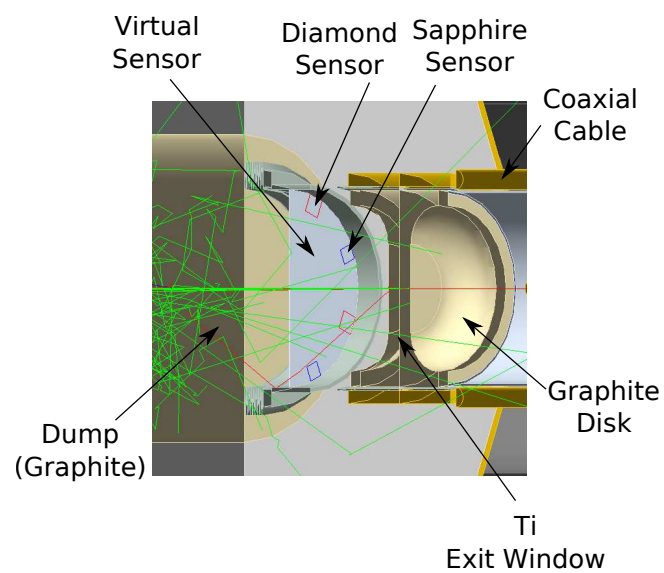


Figure 5: Enlarged view of the region between the exit window and beam dump. Note that the sensors do not have copper cups and they are located closer to the dump as in reality.

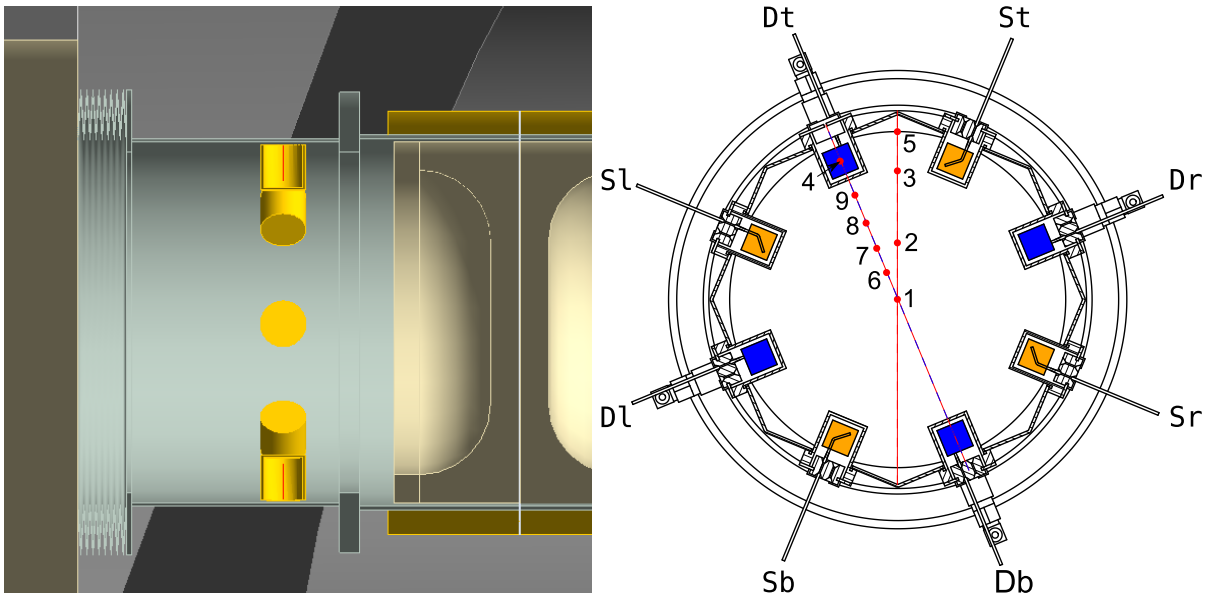


Figure 6: Geant4 model (left) and positions of the electron beam in the sensor plane (red points 1–9 on the right plot). The sensors are shown as squares in blue for diamond and orange for sapphire.

number of primary electrons was  $10^6$ . Therefore, the simulation results were normalized per 1 million primaries or 1 primary electron.

In the simulations the hadronic physics option was activated, and the QGSP-BERT hadronic physics list was used. The production rate of secondary protons and neutrons was estimated. For instance, in case of 20 mm vertical beam offset, approximately 14 neutrons and less than 1 proton per one million primary electrons impinge on the top diamond sensor. So for the results here, only electrons, positrons and photons are of interest.

As start position of the electron beam the center of the sweeper was chosen, the location of the sweeper is depicted in Fig. 1. The distance between sweeper center and front surface of dump is 2964 mm.

### 3.1 Simulation of diamond and sapphire sensors

To probe the potential response of diamond and sapphire sensors, four options of beam positions were studied, they are visualized in the right part of Fig 6:

1. The beam follows the vacuum pipe axis and has no offset in the sensor plane (point 1 in Fig. 6) .
2. The beam has a 20 mm vertical (Y) offset in the sensor plane (point 2 in Fig. 6). This corresponds to a snap-shot using a sweeper with 20 mm radius.
3. An offset of 46 mm<sup>1</sup> in vertical direction is considered (point 3 in Fig. 6). This is the maximum offset without the possibility to hit the sensors including the cups surrounding them.
4. The beam passes through the center of one (diamond, top) sensor (point 4 in Fig. 6).
5. The beam is 63 mm offset and hits the flange located near the sensors; this option corresponds to point 5 in Fig. 6).

<sup>1</sup>without cups the coordinates of this point correspond to an offset of 52 mm.

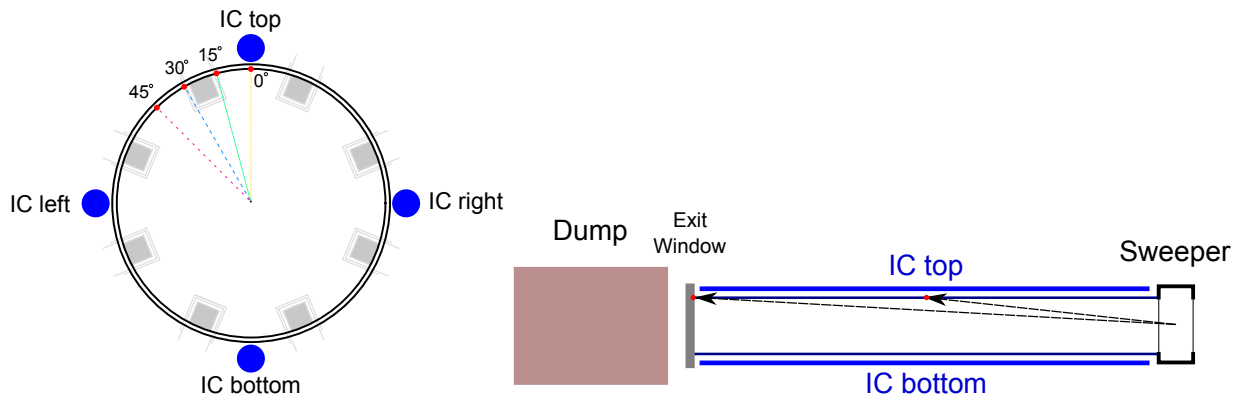


Figure 7: Geant4 model in the  $(x, y)$  plane (schematic view downstream from sweeper) and path of the electron beam if it hits the wall. The positions of the diamond and sapphire sensors downstream the exit window are given in light grey color.

6. In addition, the points 6, 7, 8 and 9 are considered assuming a Gaussian distributed beam with  $\sigma_x = \sigma_y = 3$  mm. The beam crosses the sensor plane 1 cm, 2 cm, 3 cm and 4 cm off axis on a fictitious line between top diamond sensor and sensor plane center.

By passing the exit window and the graphite disks, the electron beam induces secondary particles - mainly electrons, positrons and photons. Primary and secondary particles hit the dump and are scattered, or they create new particles. So, in all cases (1)–(4) particles hit the sensors. The number of the particles in the sensors compared to the number of electrons in the primary beam are a measure for the beam position. Since it is difficult to explicitly implement a reliable halo distribution, ideal beams were studied. The enlargement of the beam due to scattering in the exit window was considered as halo.

The sensors are shielded with copper cups. The simulations were performed including these cups but for reference purposes some simulations were also done without them.

### 3.2 Simulation procedure for ionization chambers

If the beam is lost or misdirected, particles cross the beam pipe and create showers. The shower particles are detected with ionization chambers. For the simulation it was assumed that the electron beam passes the center of the sweeper and is deflected by 41 mrad with respect to the pipe axis so that it hits the pipe in the middle between sweeper and exit window. Four points of impact were considered as shown in Fig. 7, they correspond to  $0^\circ$ ,  $15^\circ$ ,  $30^\circ$ , and  $45^\circ$  deflection in the  $(x, y)$  plane. For the simulations a Gaussian beam profile with  $\sigma = 3$  mm was assumed.

## 4 Results

To achieve enough statistics, the simulations were performed in five runs, the resulting distributions were averaged. The presentation of the results is organized as follows: The passage of particles through the sensors are discussed first. Subsequently the results for particles crossing the ionization chamber are presented.

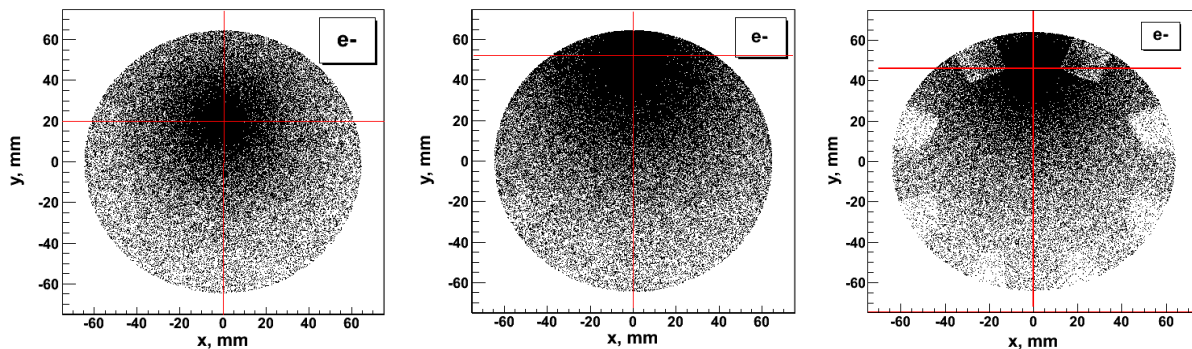


Figure 8: Electron distribution in the sensor plane for selected beam positions: 20 mm vertical offset (left) and 52 mm (middle). In the simulations for right plot the offset is 46 mm and the copper cups are included. The beam position is indicated by the red lines.

## 4.1 Simulation results for diamond and sapphire sensors

### 4.1.1 Beam cross section after the exit window

To control the beam position in the sensor plane, all electrons crossing the virtual detector plane were counted. Figure 8 shows for a setup without cups the  $(x, y)$  position of electrons crossing the sensor plane; vertical beam offsets of 20 mm (left) and 52 mm (middle) were considered. The corresponding position of a pencil-like beam in the sensor plane is indicated as intersection of two red lines. The right plot shows the simulation of the setup with copper cups assuming a vertical offset of 46 mm.

The beam size is enlarged due to scattering processes in the exit window, in addition electrons backscattered from the dump also cross the sensor plane. The distribution of electrons passing the sensor plane is shown in Fig. 9 for the four selected beam positions assuming a pencil-like and a Gaussian beam profile. The size of the initially pencil-like beam is increased to  $\sigma = 0.4$  mm for the 'centered' beam and up to  $\sigma = 0.8$  mm for a beam passing the thicker part the graphite disks of the exit window. Accordingly, a Gaussian distributed beam is broadened as shown in Fig. 9 for  $\sigma_{x,y} = 3$  mm.

The impact of copper cups on the number of electrons crossing the diamond sensors,  $N_{e^-}^D$  (the subscript  $D$  indicates the diamond sensor), can be obtained in Fig. 10. The upper three plots refer to the model without copper cups, the lower three plots result from simulations including the cups. With cups low energetic particles are cutted and cannot hit the sensors. Hence, the cups protect the sensors and improve the "signals": The ratio of the numbers of electrons registered in opposite sensors increases substantially with cups if the beam is off axis. For instance, the ratio  $N_{e^-}^{Dt}/N_{e^-}^{Db} = 3.6$  ( $t$  =top,  $b$  =bottom) without cups is 5 times smaller than with cups,  $N_{e^-}^{Dt}/N_{e^-}^{Db} = 17.4$ .

### 4.1.2 Particle distributions in the sensors

The angular distributions for electrons passing the diamond sensors are shown in Figs. 11 and 12 for two options: the primary beam runs on the beam pipe axis and the primary beam hits the virtual detector plane in point (3) of Fig. 4 (corresponds to a sweeping radius 4.6 cm). The intensity of the electron flux in forward direction (positive angles) is much higher than the intensity in backward direction, the so-called back-splash from the dump. If there is no beam offset, all sensors are hit by the same amount of particles, so Fig. 11 presents the electron flow integrated over all diamond sensors. Figure 12 presents the angular distribution of electrons crossing the top diamond detector for the case of  $\sim 50$  mm vertical offset of the primary electron

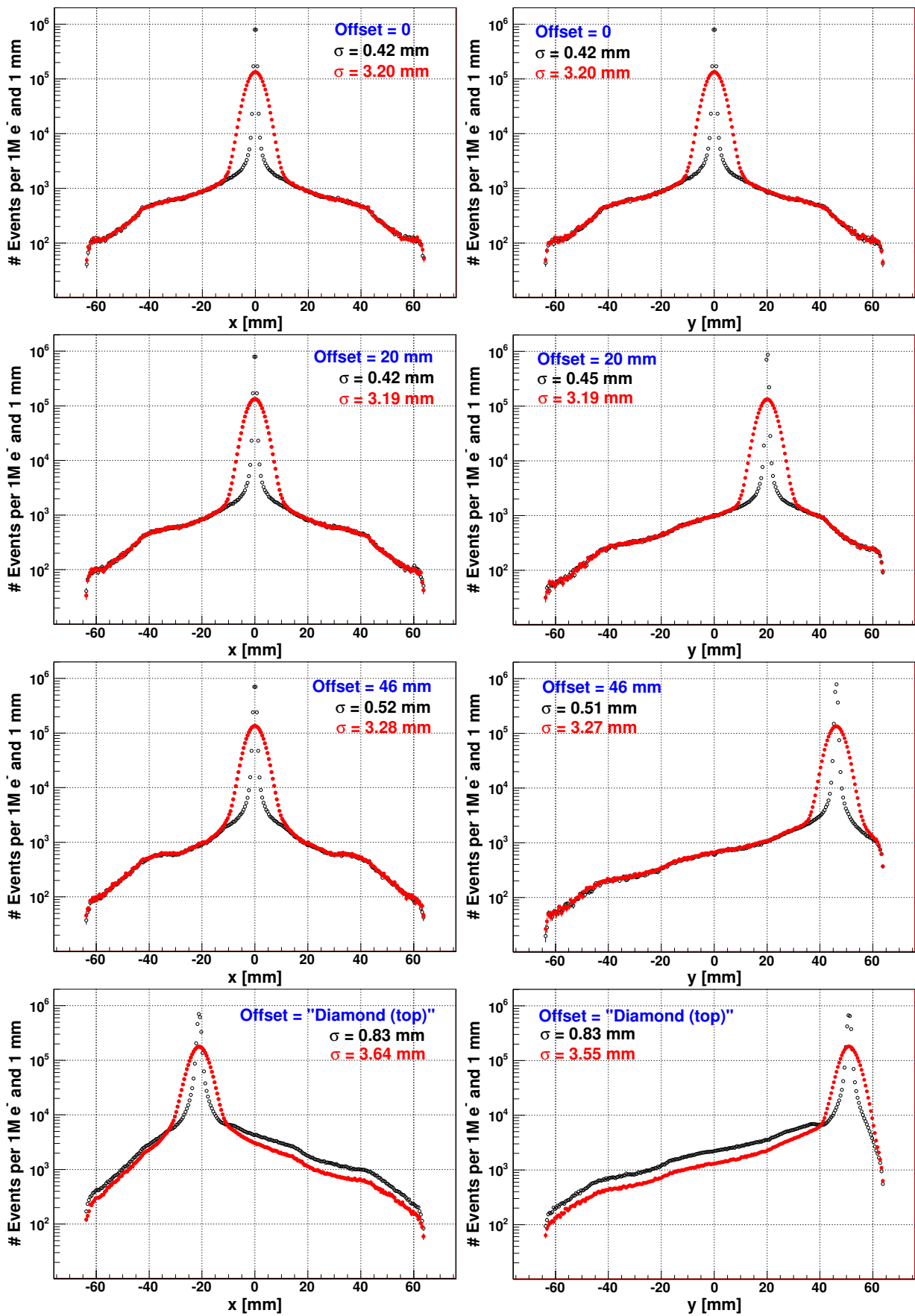


Figure 9: Electron distribution along the  $x$  and  $y$  axis of the sensor plane for selected beam positions and assuming a pencil-like and a Gaussian beam profile. The offsets 0, 20 mm, 46 mm and 'Diamond (top)' correspond to points 1, 2, 3, and 4 in Fig. 6.

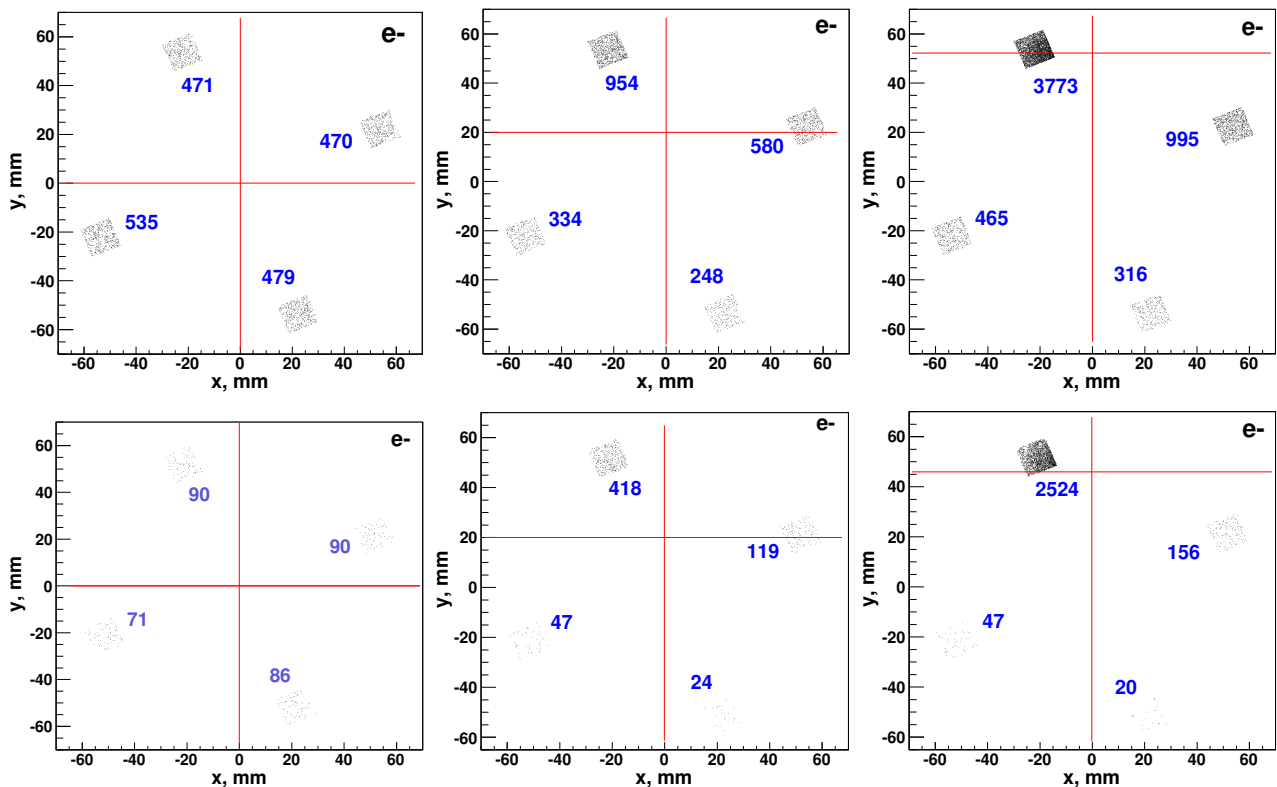


Figure 10: Number of electrons crossing the sensors after dumping  $10^6$  primary electrons of energy 1 GeV: The upper row shows the results without copper cups, the lower row with cups. The position of the primary beam is indicated by intersection of red lines.

beam.

The amount of positrons crossing the sensors is substantially smaller than the amount electrons, roughly by one order of magnitude. Nevertheless, the positron flow is included in the sensor “signals”. The contribution of neutral particles (photons and neutrons) and protons to the detector signals is ignored.

Let’s consider electrons and positrons that deposit energy in the sensors. Their spectra are shown in Figs. 13 – 16 (left plots) for four different primary beam offsets. The average energy deposition ( $\langle E_{dep} \rangle$ ) given in the box on these plots is normalized to one primary electron.

If the primary beam has no offset to the beam pipe axis, an equal energy deposition in the sensors of the same material is obtained and Fig. 13 summarizes the data averaged over four sensors. For the beam offsets 20 mm and 46 mm, the signals in the top and bottom diamond detectors are presented in Fig. 14 and 15. In the case that the primary beam goes through the center of the top diamond sensor, the response of this detector is shown in Fig. 16. The full information about the intensity of flow through diamond and sapphire sensors and the energy deposited in each sensor is collected in Table 5. The detailed results are given for a pencil-like beam, for comparison also the energy deposition in the sensors is shown for a Gaussian beam profile with  $\sigma_x = \sigma_y = 3$  mm.

It is interesting to see that the beam size affects the energy deposition in the sensors only slightly. The sensor signals rise only substantially if the beam comes very close sensor and the surrounding cups. Table 2 shows the average energies deposited per primary 1-GeV electron in the sensors for further beam positions off axis assuming a Gaussian beam with  $\sigma_x = \sigma_y = 3$  mm.

The results of the Geant4 simulations were saved in ROOT files, all information about position, energy and angle of any particle crossing the detectors was saved individually for each sensor. The distribution of energy deposited in the sensors was saved in a separate

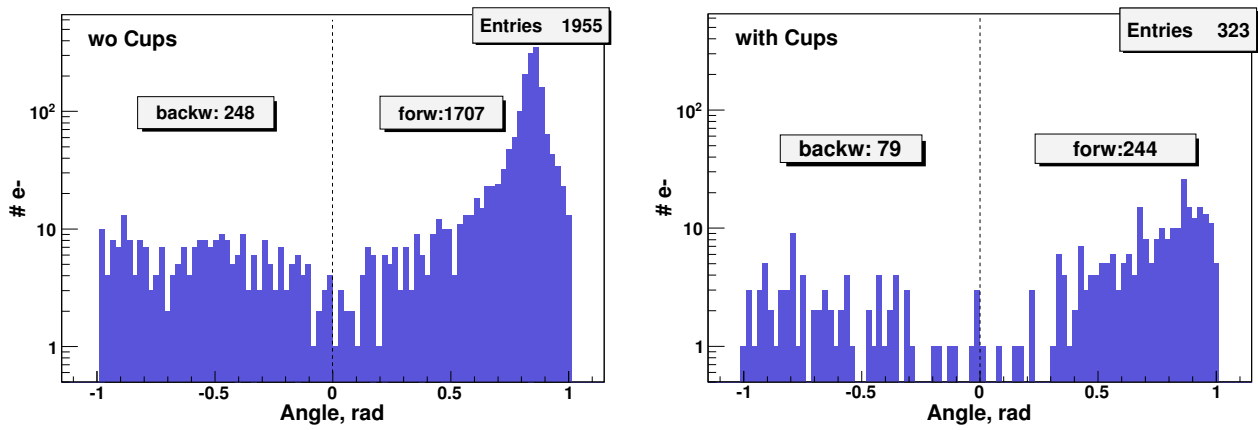


Figure 11: Angular distribution of electrons crossing the diamond sensors without cups (left) and with cups (right). The primary beam has no offset (point 1 in Fig. 6). The distribution is integrated over all four sensors.

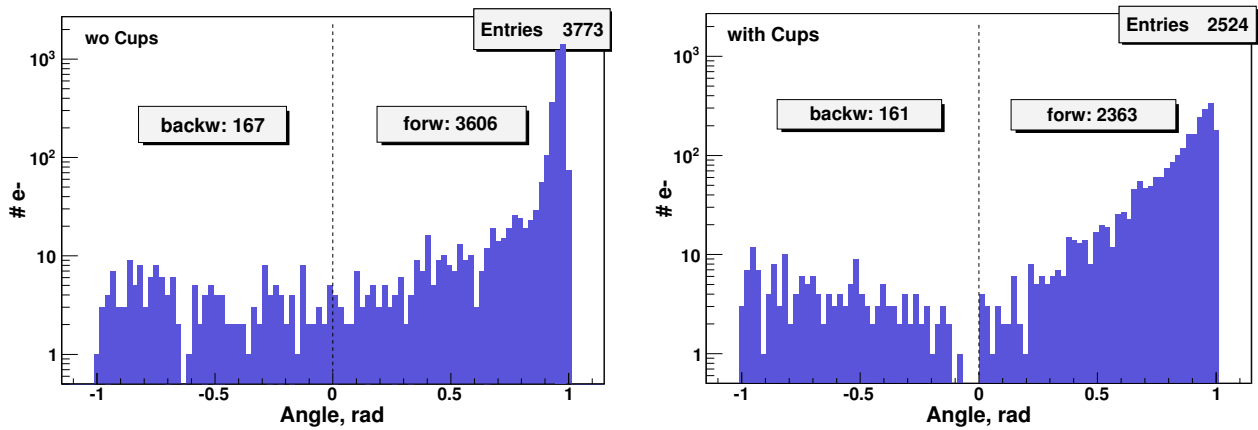


Figure 12: Angular distribution of electrons crossing the top diamond sensor without cups (left) and with cups (right). The primary beam has a vertical offset corresponding to point 3 in Fig. 6.

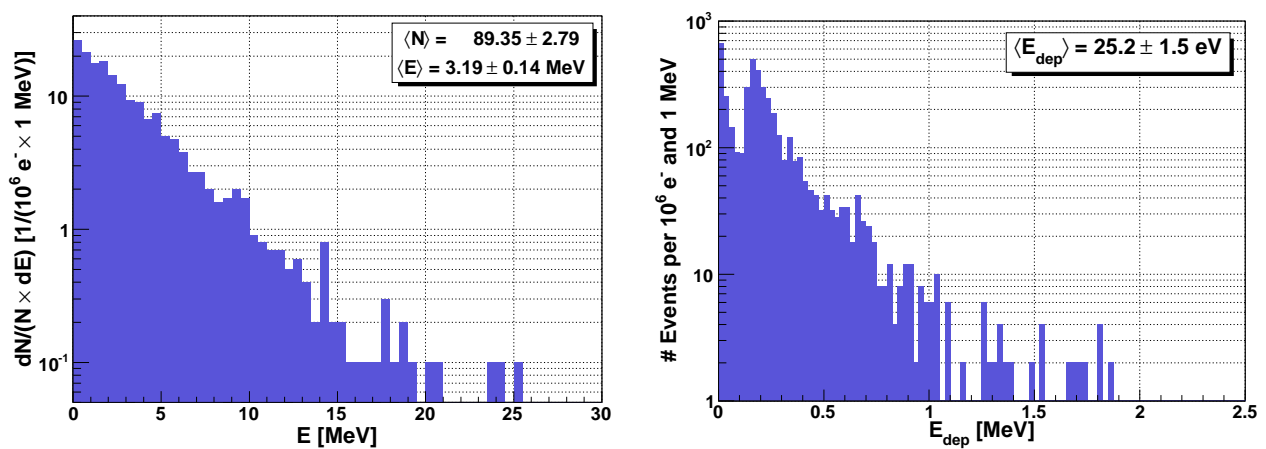


Figure 13: Energy distribution of electrons crossing the diamond sensors (left) and energy deposition in the diamond sensors (right). The primary beam has no offset (point 1 in Fig. 6), the sensors are embedded in cups.

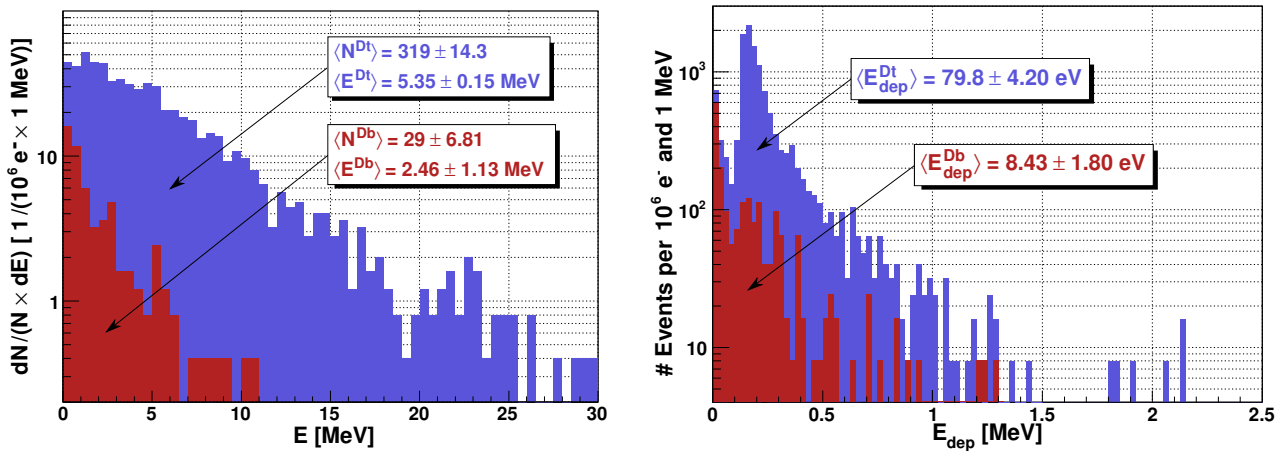


Figure 14: Energy distribution of electrons (left) and energy deposition (right) in the top (t) and bottom (b) diamond sensors. The primary beam has 20 mm vertical offset (point 2 in Fig. 6), the sensors are embedded in cups.

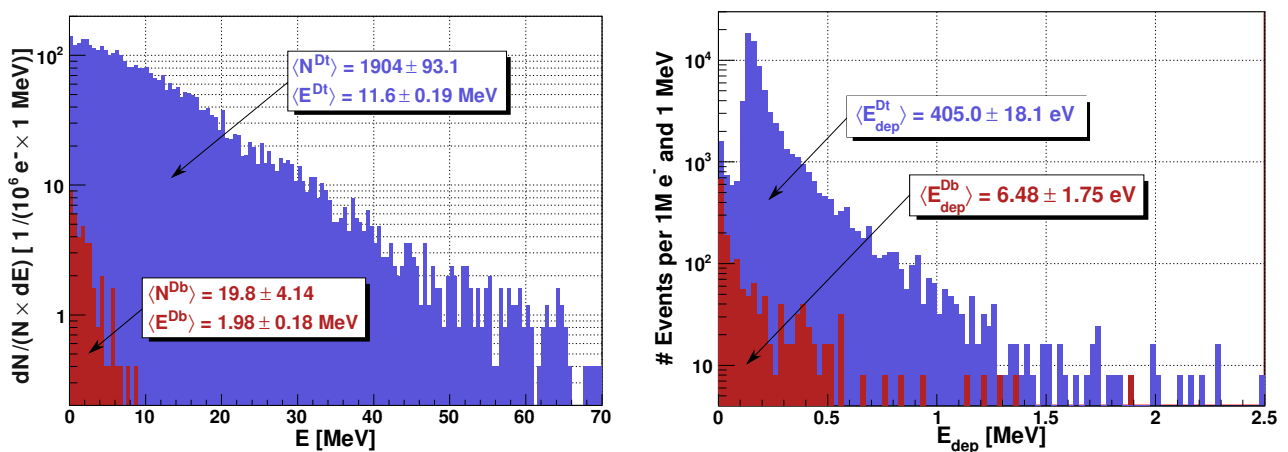


Figure 15: Energy distribution of electrons (left) and energy deposition (right) in the top (t) and bottom (b) diamond sensors. The primary beam has 46 mm vertical offset (point 3 in Fig. 6), the sensors are embedded in cups.

Offset [mm]	Sensor	$N_e$ per $10^6 e^-$	$\sigma_N$ [%]	$\langle E_e \rangle$ [MeV]	$\sigma_{\langle E \rangle}$ [%]	$\langle E_{dep} \rangle$ [eV/prim]	$\sigma_{\langle E_{dep} \rangle}$ [%]	$\langle E_{dep} \rangle$ [eV/prim]	$\sigma_{\langle E_{dep} \rangle}$ [%]
“pencil-like beam”								$\sigma_x = \sigma_y = 3 \text{ mm}$	
—Diamond sensors—									
0	all	89.3	3.1	3.2	4.5	25.2	6.1	24.3	6.4
20 (point 2)	top	319.0	4.5	5.4	2.9	79.9	5.3	83.0	9.7
	bottom	29.0	23.5	2.5	45.9	8.4	21.4	8.5	8.3
	right	122.8	6.6	3.6	12.7	35.2	8.5	34.1	10.6
	left	44.8	19.0	3.3	13.7	12.2	25.5	13.9	18.2
46 (point 3)	top	1904.0	4.9	11.7	1.7	405.0	4.5	437.9	2.1
	bottom	19.8	20.9	2.0	9.3	6.5	27.1	6.6	13.5
	right	130.6	7.1	3.4	7.4	38.1	12.7	37.7	12.0
	left	37.4	6.4	2.0	17.6	10.2	11.5	11.3	28.3
55 (point 4)	top	$1.3 \cdot 10^6$	0.03	555.2	0.05	$2.2 \cdot 10^5$	0.07	$1.9 \cdot 10^5$	0.11
	bottom	45.0	22.1	1.5	21.3	14.3	22.4	17.3	13.7
	right	130.4	7.6	2.3	7.4	43.9	16.9	45.8	5.6
	left	150.6	10.7	2.1	2.7	52.4	18.2	46.9	12.4
—Sapphire sensors—									
0	all	65.3	7.8	3.4	4.0	31.1	9.4	29.8	9.4
20 (point 2)	top	235.0	10.6	5.2	7.4	100.4	9.4	99.6	5.9
	bottom	22.2	14.0	2.3	19.2	11.7	24.2	10.6	23.3
	right	34.0	24.8	2.9	9.7	15.9	25.8	17.0	22.9
	left	78.6	8.5	4.2	15.9	38.5	9.5	40.0	16.6
46 (point 3)	top	1356.4	2.9	11.4	1.9	509.2	2.9	549.8	2.4
	bottom	15.6	31.6	1.6	26.5	7.3	24.7	8.0	49.8
	right	23.8	14.7	1.8	25.6	10.9	30.9	16.1	21.6
	left	102.6	14.3	3.5	15.9	48.2	14.2	48.6	5.0
55 (point 4)	top	583.4	5.4	4.6	7.9	287.2	5.9	287.3	2.4
	bottom	40.0	8.8	1.7	13.0	21.5	16.8	25.0	11.8
	right	42.2	22.7	2.0	64.9	19.9	24.4	28.2	13.6
	left	582.2	2.6	4.5	5.3	289.3	5.6	277.7	5.1

Table 1: Simulation results for diamond and sapphire sensors, both enclosed in cups, assuming a pencil-like beam. For comparison, the average energy deposition per primary 1-GeV electron is also given for a Gaussian beam profile. The offsets 0, 20 mm, 46 mm and 55 mm correspond to points 1, 2, 3, and 4 in Fig. 6.

			Diamond sensors		Sapphire sensors	
Offset [mm]	Angle [deg]	Sensor	$\langle E_{dep} \rangle$ [eV/prim]	$\sigma_{\langle E_{dep} \rangle}$ [%]	$\langle E_{dep} \rangle$ [eV/prim]	$\sigma_{\langle E_{dep} \rangle}$ [%]
10 (point 2)	-22.5	top	48.4	20.3	47.4	4.6
	-22.5	bottom	15.7	7.8	17.2	12.0
	-22.5	right	23.0	7.8	21.6	20.4
	-22.5	left	25.2	23.5	42.3	8.1
20 (point 7)	-22.5	top	99.8	6.6	71.0	13.8
	-22.5	bottom	9.2	39.9	14.8	15.6
	-22.5	right	19.5	27.9	10.9	11.2
	-22.5	left	23.8	13.0	71.3	9.8
30 (point 8)	-22.5	top	217.6	6.0	90.1	5.9
	-22.5	bottom	6.4	36.9	7.8	19.1
	-22.5	right	16.9	28.0	7.5	26.4
	-22.5	left	19.1	25.8	96.3	4.5
40 (point 9)	-22.5	top	1550.2	1.2	121.7	4.3
	-22.5	bottom	7.9	27.2	5.6	27.2
	-22.5	right	17.6	14.1	8.8	24.7
	-22.5	left	17.0	25.5	120.0	5.2
63 (point 5)	0	top	7179.3	1.0	8904.4	0.5
	0	bottom	331.4	2.6	396.8	3.2
	0	right	883.8	4.1	549.7	3.1
	0	left	454.4	2.1	1108.0	1.7

Table 2: Average energy deposited per 1-GeV primary electron in diamond and sapphire sensors, both enclosed in cups. A Gaussian beam profile is assumed,  $\sigma_x = \sigma_y = 3$  mm. The offsets 10 mm, 20 mm, 30 mm, 40 mm, and 63 mm correspond to points 6, 7, 8, 9, and 5 in Fig. 6.

ROOT tree. These data can be used later on for comparison and interpretation of experimental results.

Figures 17 and 18 summarize the intensities of the particle flow through the sensors and the energies deposited in the sensors, which are strongly correlated. For the sweeping option resulting in 20 mm beam offset, the ratios between the strongest (top) and weakest (bottom) sensor “signals” are  $N_e^{Dt}/N_e^{Db} = 11.0$ ,  $E_{dep}^{Dt}/E_{dep}^{Db} = 9.5$  for diamond sensors, and  $N_e^{St}/N_e^{Sb} = 10.6$ ,  $E_{dep}^{St}/E_{dep}^{Sb} = 8.5$  for sapphire sensors. Assuming that the sensitivity is given by the energy deposition, the sensitivity of sapphire and diamond sensors is similar.

### 4.1.3 Interpretation of results

By comparing the number of electrons and positrons passing the sensor plane (Tab. 5) with the electron distribution along the  $x$  and  $y$  axis (Fig. 9), it is pointed out that the signals in the sensors depend strongly on the halo distribution which is not known in practice. However, to interpret the results, the average energy deposited in the sensors is normalized to one primary beam electron. This allows to evaluate the dynamical range. If the beam profile would be known, expectations for realistic measurements could be derived by folding the simulation results for an ideal beam with the actual beam profile.

#### Average energy deposition in the sensors

Based on the simulation results for a pencil-like beam, the average energy deposited in the sensors surrounded by copper cups can be related to the distance between sensor and beam. This simulated calibration curve is presented in Fig. 19. This curve is only valid if the beam does not hit a sensor directly or crosses the flange. In the latter cases additional particles are created in the copper cups, flange and beam pipe material, and seen by the other sensors and the energy deposition in the sensors is much higher as depicted in Fig. 19. The (simulated) calibration curve is not linear.

#### Reconstruction of beam position

Since neither the realistic beam profile including the halo nor the sensor response are taken into account, only qualitative conclusions are possible to indicate that the beam hits the central part of the dump.

If the beam hits a sensor, the signal is huge and the detection of a misdirected beam is easy. In the other cases, a rough guess of the beam position can be done easily, but the precise reconstruction is difficult because of the following facts:

- The particle distribution in the realistic beam halo is not known.
- The sensors detect only a part of the halo.
- The halo distribution in the sensor plane depends also on the beam position: Fig. 9 shows an asymmetric distribution for beams off axis due to the outward growing thickness of the graphite disks at the exit windows.
- The calibration of the sensors is essential.

To ensure that the beam is kept within the required range, the sensor signals should be relatively small, their variations must not exceed certain limits (to be calibrated) and should follow the sweeping frequency. Based on the more or less ideal beam used for the studies and assuming that the average energy deposition is proportional to the sensor signal, rough estimates of such limits could be:

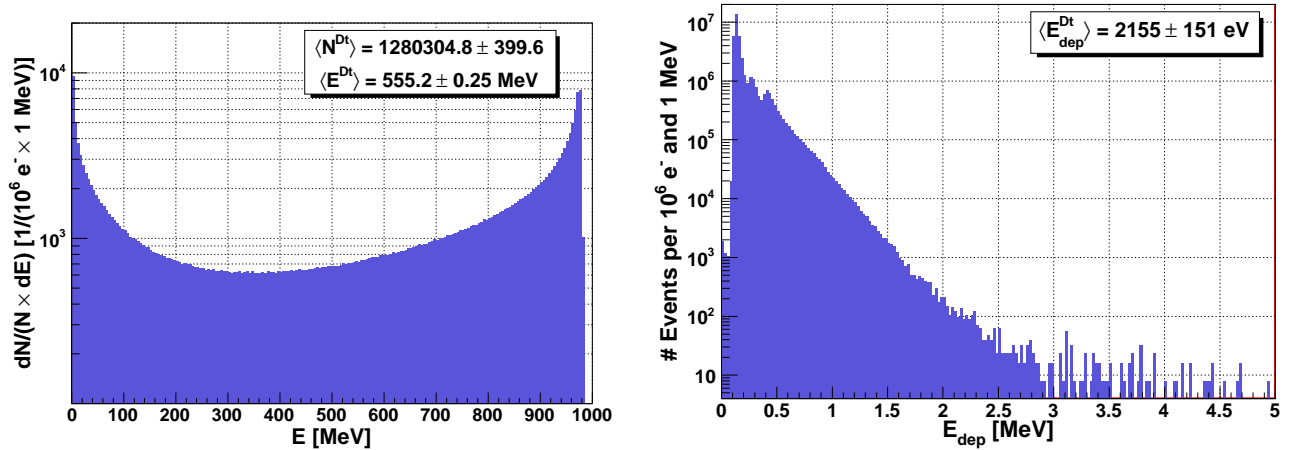


Figure 16: Energy distribution of electrons (left) and energy deposition (right) in the top diamond sensor. The primary beam passes the center of the top diamond sensor (point 4 in Fig. 6), which is embedded in a copper cup.

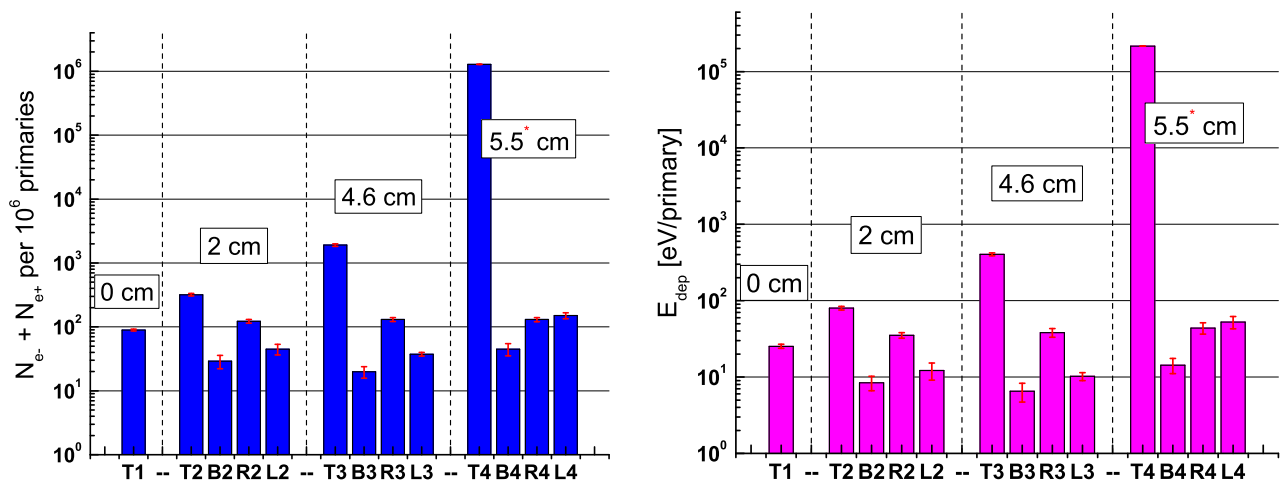


Figure 17: Number of electrons and positrons passing through the diamond detectors (left) and energy deposited in diamond sensors (right). The sensors are identified by the letters T (top), B (bottom) L(left), R(right), and the beam offset is described by the the numbers  $i = 1 \dots 4$  corresponding to points 1, 2, 3, and 4 in Fig. 6. The sensors are embedded in copper cups.

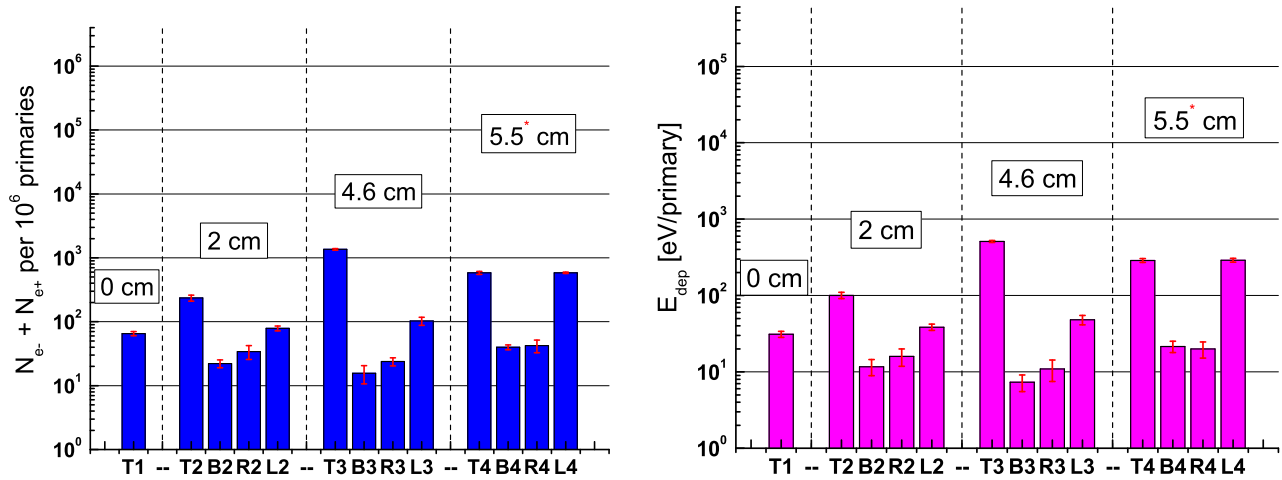


Figure 18: Number of electrons and positrons passing through the sapphire detectors (left) and energy deposited in sapphire sensors (right). The sensors are identified by the letters T (top), B (bottom) L(left), R(right), and the beam offset is described by the the numbers  $i = 1 \dots 4$  corresponding to points 1, 2, 3, and 4 in Fig. 6. The sensors are embedded in copper cups.

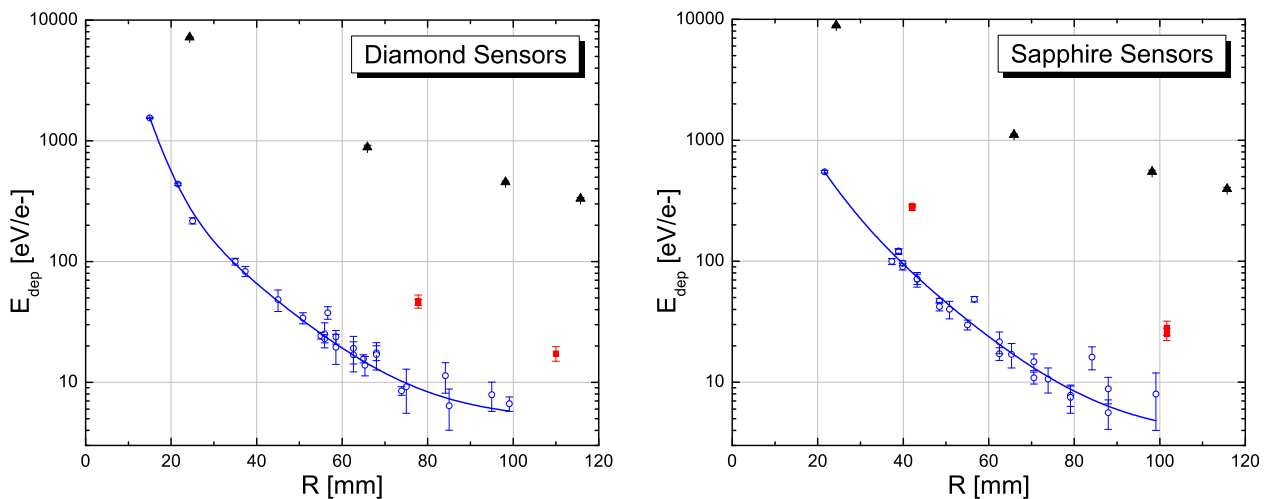


Figure 19: Average energy,  $\langle E_{dep} \rangle$ , deposited in the sensors per 1-GeV electron surrounded by copper cups as function of the distance  $R$  between sensor and beam. If the beam hits a sensor (red 'data' points) or the flange near the sensors (black 'data' points), which corresponds to the offsets 4 and 5 in Fig. 6, the energy deposition in the sensors is substantially higher.

- A factor of about 10 to 12 in the energy deposition of opposite sensors is the maximum acceptable difference, otherwise the beam is very close to the sensors.
- It might be useful to introduce a measure  $M = (S1 + S2 - S3 - S4)/(S1 + S2 + S3 + S4)$  where  $S1$  and  $S2$  correspond to the energy deposition in the two neighboring sensors with the highest and second highest 'signal',  $S3$  and  $S4$  correspond to the energy deposition in the opposite sensors. The central beam or the 2-cm-swept beam yield  $M \leq 0.7$ ; if the beam comes close to the sensors  $M$  approaches values greater than 0.8.

Of course, these numbers have to be tested and revised after calibration and beam tests.

## 4.2 Simulation results for ionization chambers

Based on the simulations, the number of electrons and positrons passing through the ionization chambers were counted. Fig. 20 shows these numbers as function of the distance  $R$  between ionization chamber and point of impact of the primary beam on the inner surface of the pipe. The results are normalized per  $10^6$  primary electrons, so they can be scaled if halo particles are considered. The results are summarized in Table 3 depicted in Fig. 20. In case of  $0^\circ$  the beam passes an ionization chamber, and the number of shower particles is increased substantially.

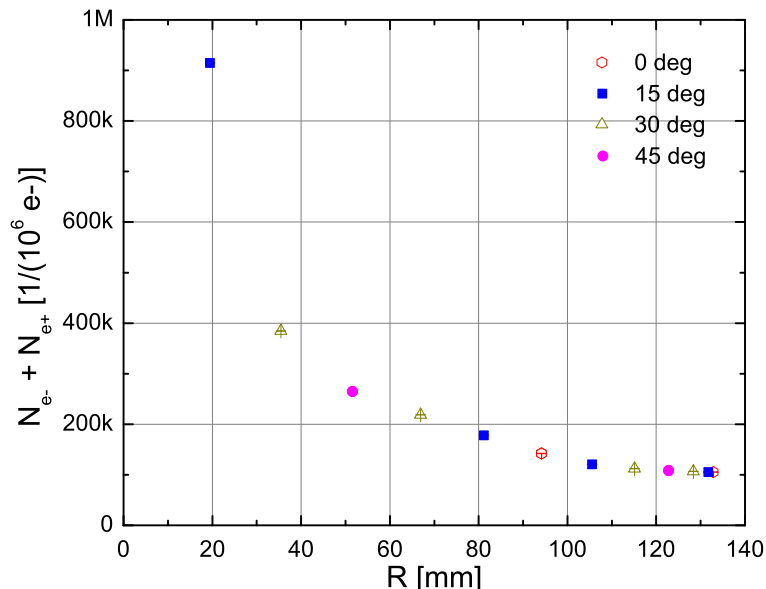


Figure 20: Number of electrons and positrons passing through the ionization chambers per  $10^6$  primary electrons as function of the distance  $R$  between sensor and beam.

The energy distribution of electrons and positrons passing the top and bottom ionization chambers is given in Fig. 21 for different angular deflections in the  $(x,y)$  plane resulting in different points of impact on the pipe.

### 4.2.1 Beam loss monitoring

The signal in the IC depends on the number of charged particles passing through. This number depends on the distance,  $N_e \sim 1/R^2$  and on the number of beam particles hitting the wall. Beam losses are indicated by higher currents in the IC, the approximate position is given by the relation among the IC signals.

If the beam is lost at the end of the beam pipe, the beam particles hit the wall, the exit window and the shower passes the flange but the signals in the IC are small. This 'worst

Angle [deg]	IC	$\langle N_e \rangle$ per $10^6$ $e^-$	$\sigma_{\langle N_e \rangle}$ [%]
0	top	3478000	0.05
	bottom	105400	0.20
	right	142300	0.10
	left	141900	0.20
15	top	914700	0.09
	bottom	105300	0.17
	right	120500	0.26
	left	177800	0.15
30	top	383800	0.06
	bottom	108200	0.34
	right	111700	0.23
	left	218100	0.27
45	top	264400	0.13
	bottom	107500	0.20
	right	108000	0.29
	left	264600	0.28

Table 3: Number of electrons and positrons passing through the ionization chambers per  $10^6$  primary electrons assuming a beam loss at the half distance between sweeper and exit window. The angular deflections in the  $(x,y)$  plane correspond to different points of impact on the pipe (see Fig. 7).

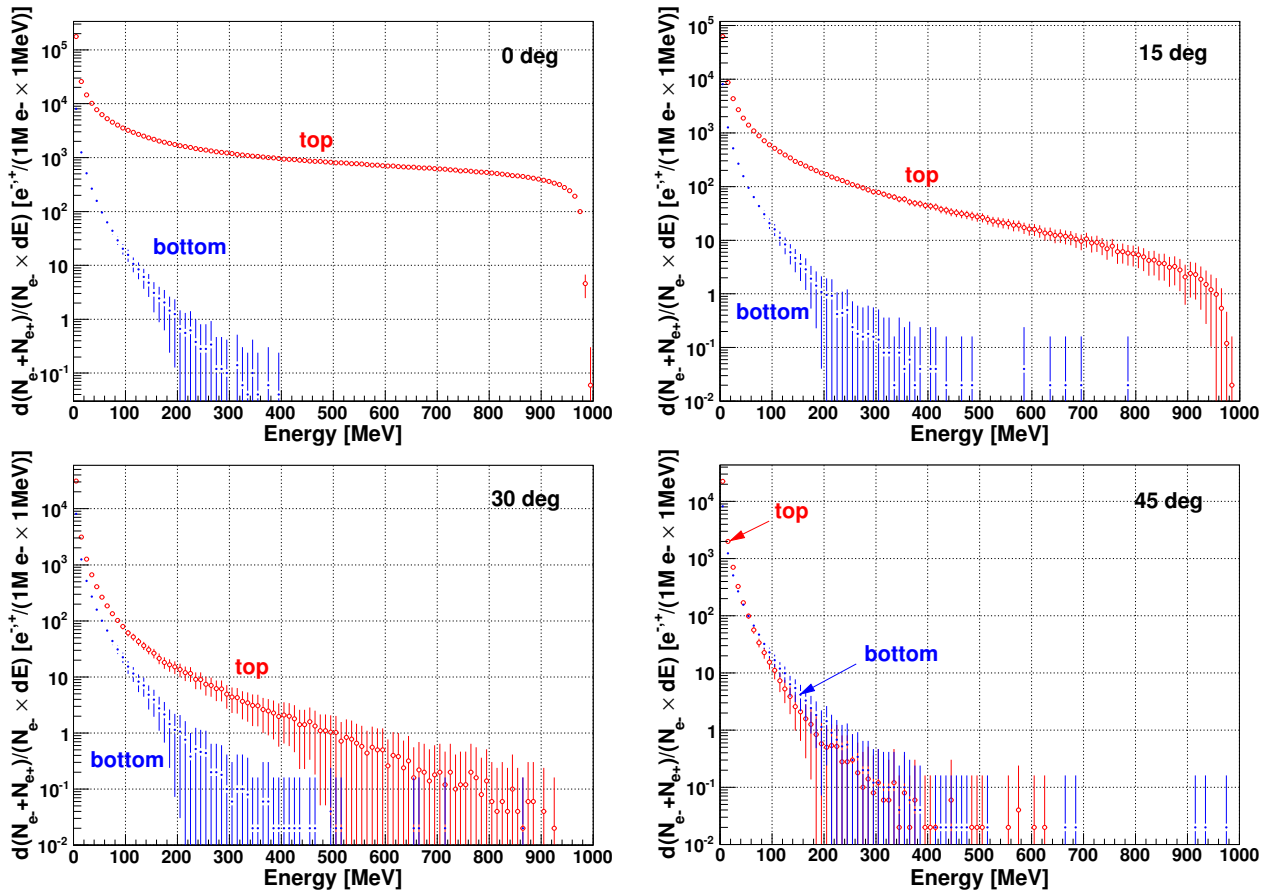


Figure 21: Energy distribution of electrons and positrons passing the top and bottom ionization chambers per  $10^6$  primary electrons assuming a beam loss at the half distance between sweeper and exit window. The angular deflections in the  $(x,y)$  plane correspond to different points of impact on the pipe (see Fig. 7).

IC	$\langle N_e \rangle$ per $10^6 e^-$	$\sigma_{\langle N_e \rangle}$ [%]
top	19600	0.41
bottom	12100	1.18
right	12000	1.21
left	19700	0.86
Diamond sensors	$\langle E_{dep} \rangle$ [eV/e <sup>-</sup> ]	$\sigma_{\langle E_{dep} \rangle}$ [%]
top	9470	0.4
bottom	440	2.4
right	500	3.7
left	1260	2.0
Sapphire sensors	$\langle E_{dep} \rangle$ [eV/e <sup>-</sup> ]	$\sigma_{\langle E_{dep} \rangle}$ [%]
top	1560	1.5
bottom	710	1.9
right	540	1.0
left	11780	1.2

Table 4: Simulation results for ionization chambers, and diamond and sapphire sensors assuming a beam loss at the end of the vacuum chamber. The beam hits the wall at  $45^\circ$  (see Fig. 7), i.e. the assumed (and extended) path of the beam cannot hit the sensors or the IC.

case' scenario was simulated assuming a beam loss at the end of the vacuum chamber at the position  $45^\circ$  (see Fig. 7). The results are summarized in Table 4: Although the IC do not see a significant signal, the diamond and sapphire sensors are passed by the shower particles. The energy deposition in the sensors near to the shower is increased significantly.

## 5 Summary

The simulation results show that the ionization chambers along the beam pipe together with the sensors downstream the exit window allow to monitor misdirection and loss of the electron beam. The design and combination of the diagnostic elements ensures that the beam impinges the dump at the required area.

## References

- [1] Geant4, <http://geant4.web.cern.ch/geant4/>

## Addendum: Energy Spectra of Photons at the End of the FLASH Dump Line

In the FLASH seminar held on 9 March 2010 it was asked what the number and the energy spectrum of the photons in the FLASH dump line is. These photons are created primarily when the electron beam passes the exit window, or hits the beam pipe or the dump. In addition, also the secondaries – the scattered electrons and positrons – can create photons. Although the number of photons created is large, they have only a minor influence on the signals in the diamond sensors in front of the dump. Thus, they have not been considered explicitly in the note above but are considered for completeness in this short addendum.

To estimate the role of these photons, the energy spectra of photons crossing the diamond sensors in front of the dump have been simulated. The average number of particles going through sensors and their energies have been calculated separately for the fluxes in forward direction (coming from the exit window) and backward direction (back-scattered from the FLASH beam dump) assuming a pencil-like primary 1-GeV-beam with 0, 20 mm and 46 mm vertical offsets as described in the note above. The results are shown in Figures 22–25 and summarized in Table 5. The total energies deposited in the diamond sensors as well as the energy depositions caused by the photons only are shown in Table 6. The photons contribute typically between 1% and 7% to the total energy deposition. The averaged energy of the backward scattered photons is relatively low, about 0.2 MeV. The number of photons outside

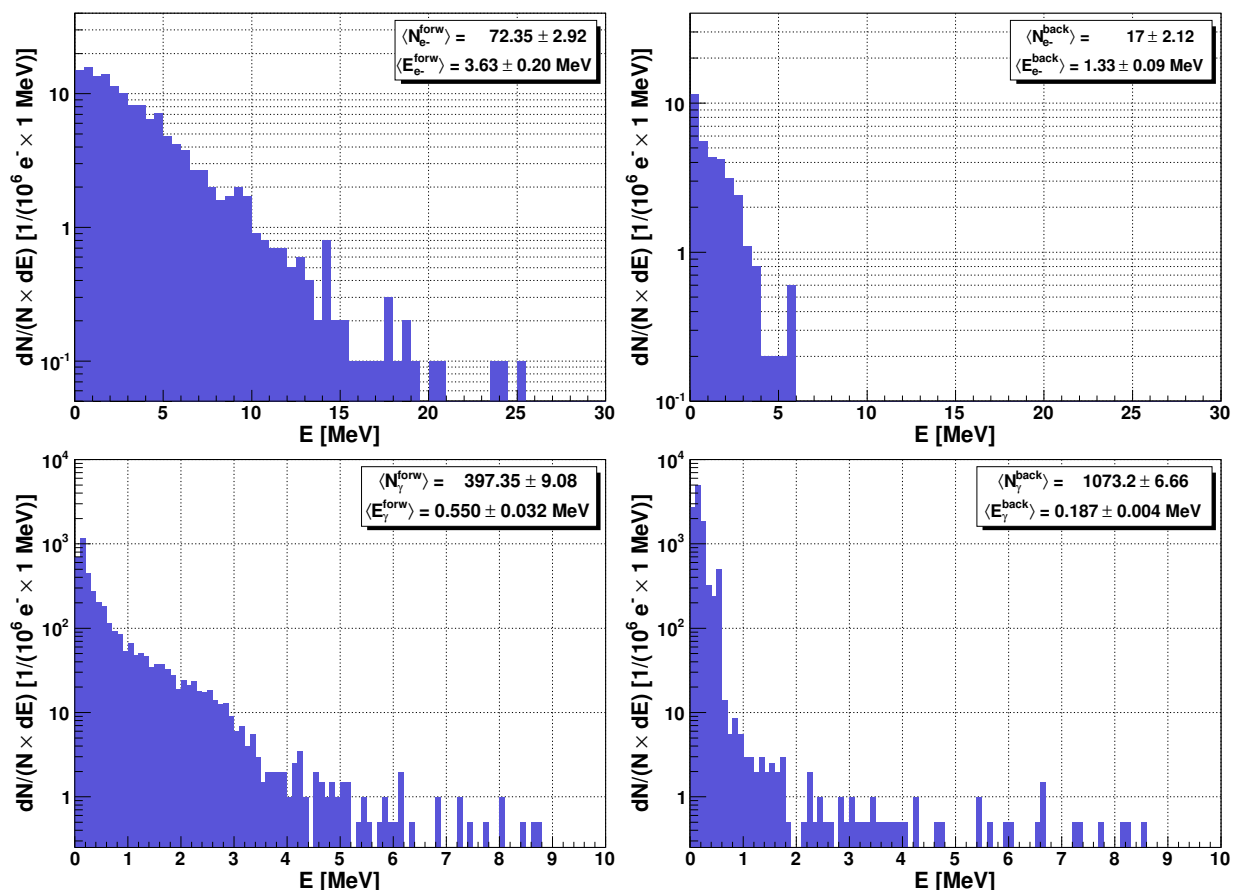


Figure 22: Energy spectra of charged particles (upper plots) and photons (lower plots) passing the plane with diamond sensors: left plots – particles come from the exit window (forward direction), right plots – particles are back-scattered from beam dump (backward direction). The pencil-like primary beam has no offset.

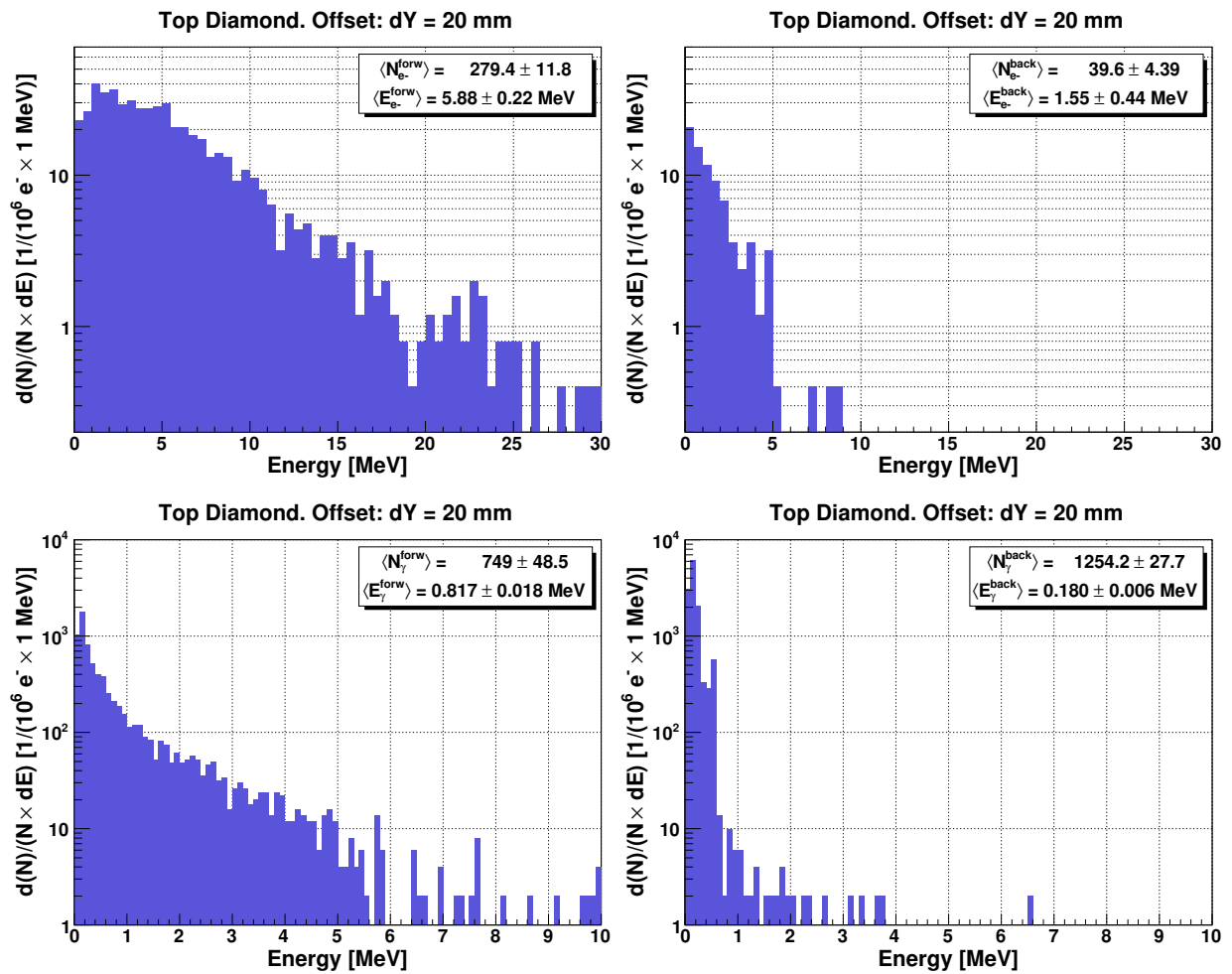


Figure 23: Energy spectra of charged particles (upper plots) and photons (lower plots) passing the top diamond sensor: left plots – particles come from the exit window (forward direction), right plots – particles are back-scattered from beam dump (backward direction). The pencil-like primary beam has 20 mm vertical offset.

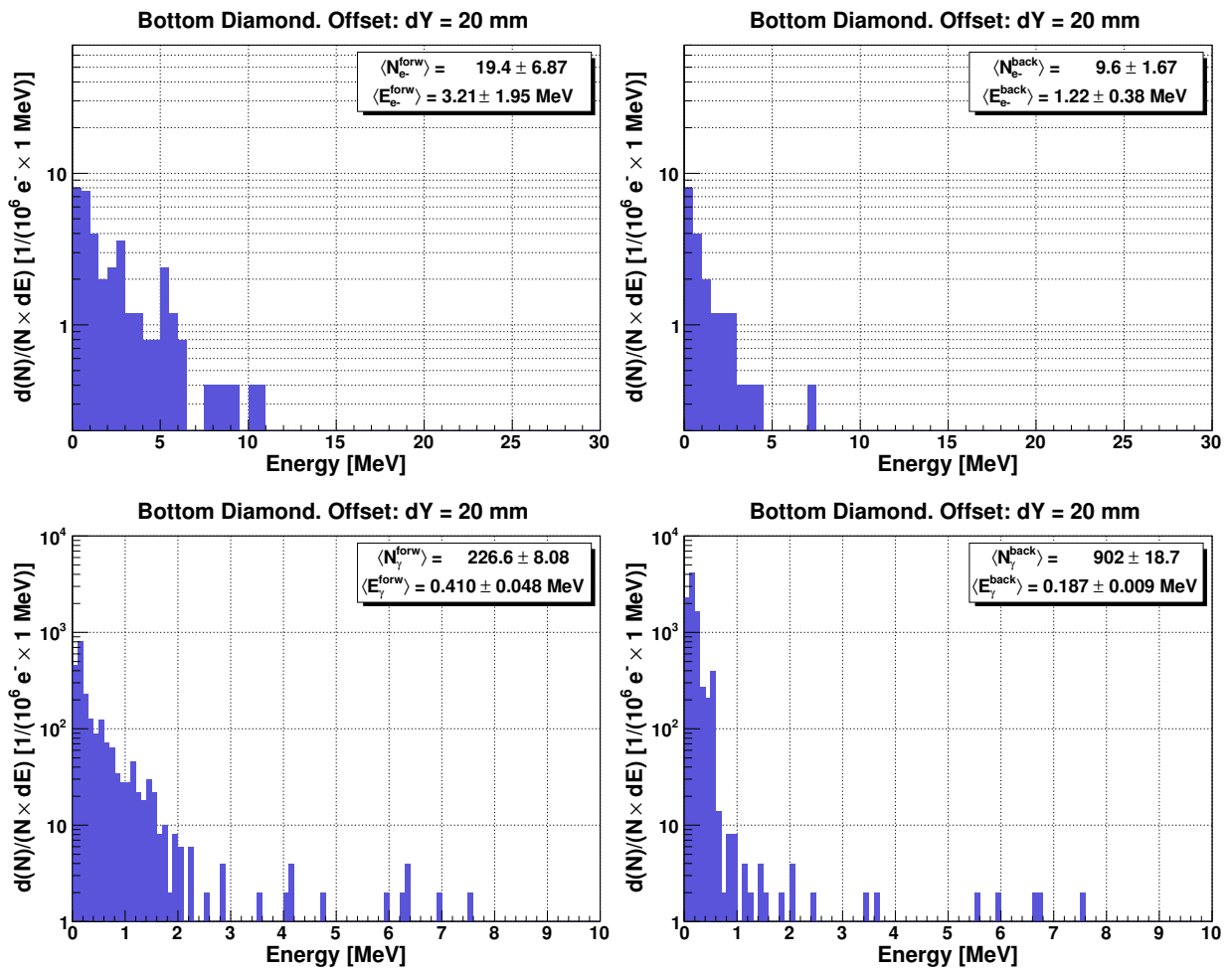


Figure 24: Energy spectra of charged particles (upper plots) and photons (lower plots) passing the bottom diamond sensor: left plots – particles come from the exit window (forward direction), right plots – particles are back-scattered from beam dump (backward direction). The pencil-like primary beam has 20 mm vertical offset.

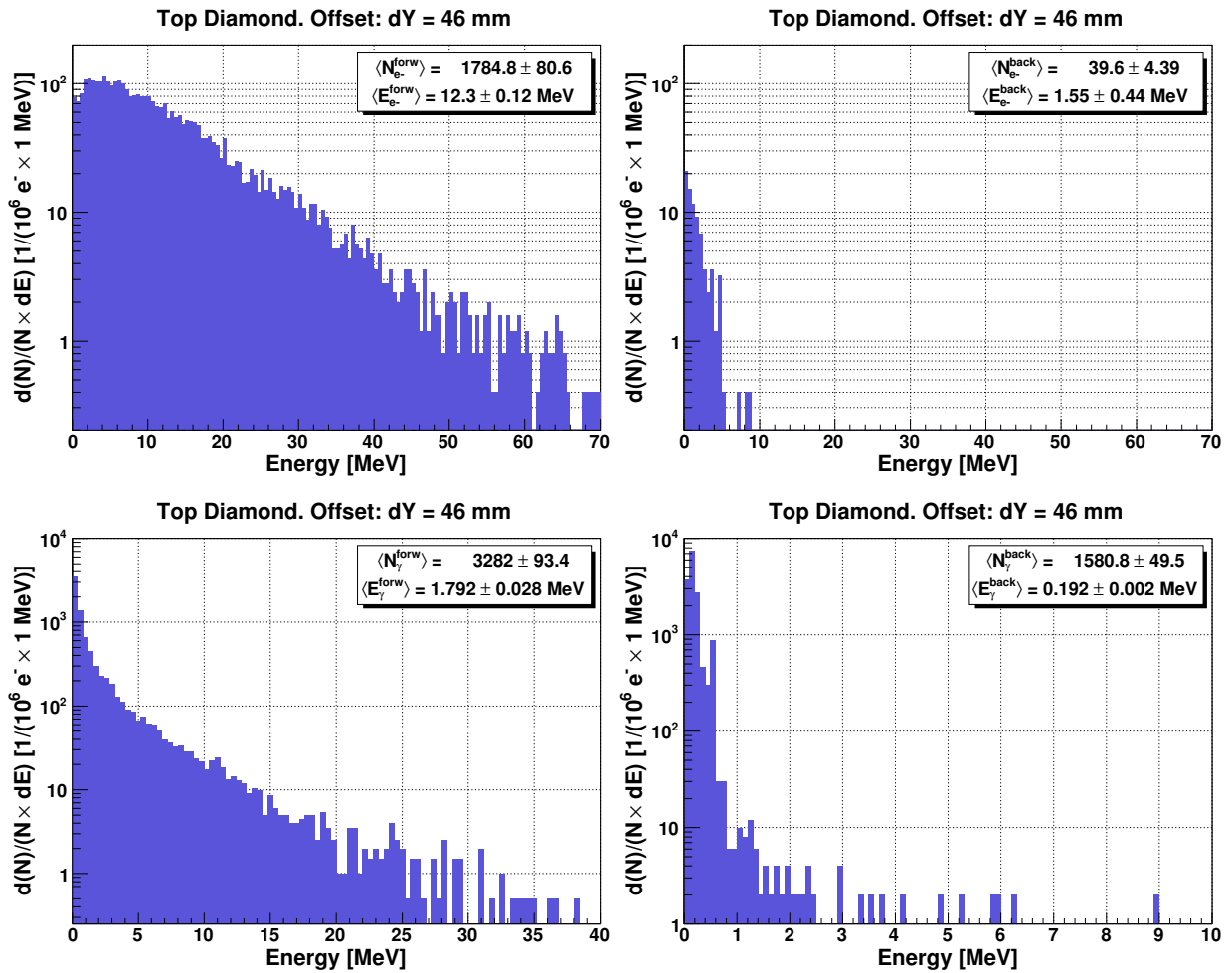


Figure 25: Energy spectra of charged particles (upper plots) and photons (lower plots) passing the top diamond sensor: left plots – particles come from the exit window (forward direction), right plots – particles are back-scattered from beam dump (backward direction). The pencil-like primary beam has 46 mm vertical offset.

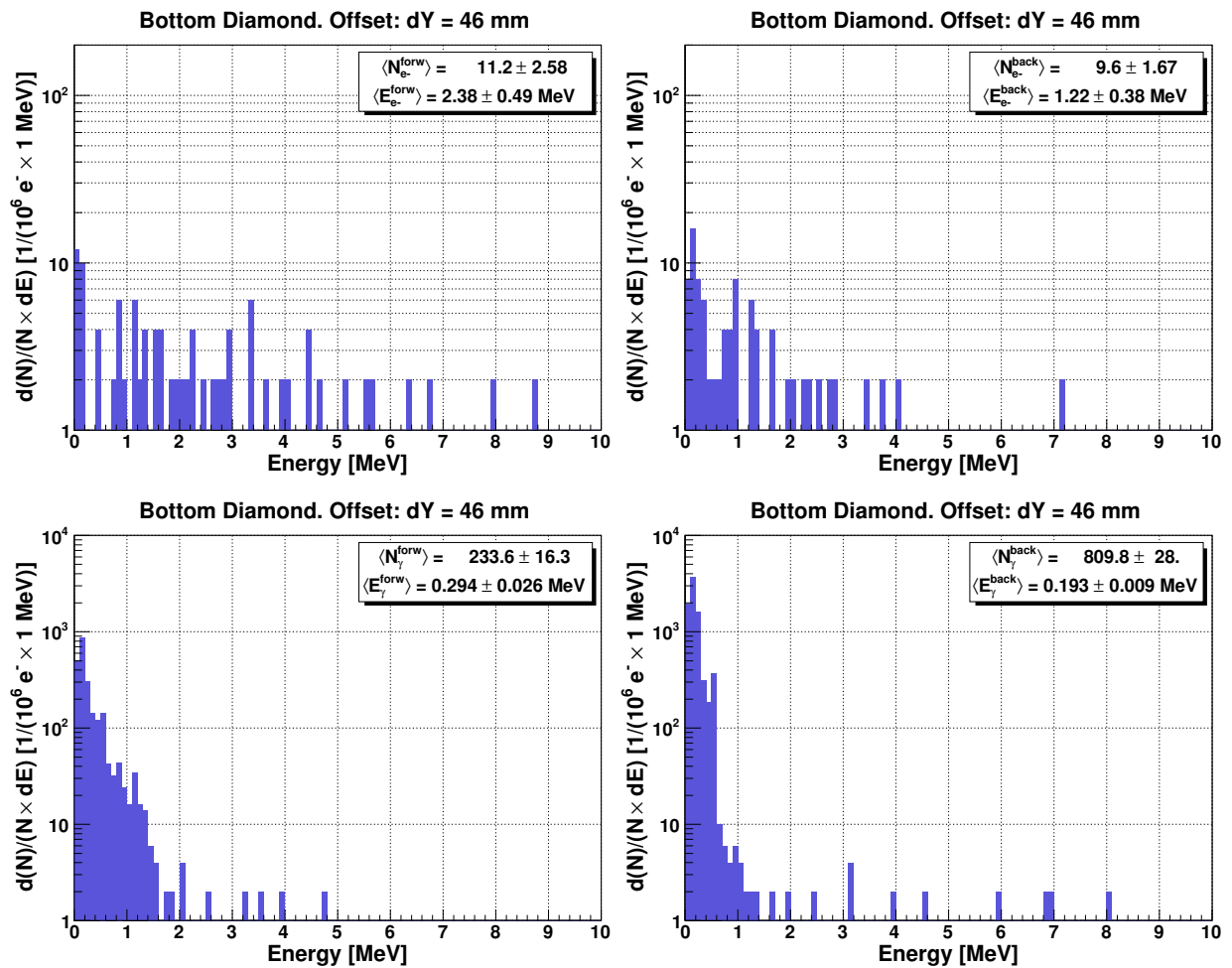


Figure 26: Energy spectra of charged particles (upper plots) and photons (lower plots) passing the bottom diamond sensor: left plots – particles come from the exit window (forward direction), right plots – particles are back-scattered from beam dump (backward direction). The pencil-like primary beam has 46 mm vertical offset.

Offset [mm]	Sensor	$N_e$	$N_\gamma$	$\langle E_e \rangle$	$\langle E_\gamma \rangle$
		per $10^6 e^-$		[MeV]	
0	t,b	$89 \pm 3$	$1470 \pm 7$	$3.2 \pm 0.1$	$0.29 \pm 0.01$
20	t	$319 \pm 14$	$2003 \pm 53$	$5.4 \pm 0.2$	$0.42 \pm 0.02$
	b	$29 \pm 7$	$1129 \pm 20$	$2.5 \pm 1.1$	$0.23 \pm 0.02$
46	t	$1904 \pm 93$	$4863 \pm 108$	$11.7 \pm 0.2$	$1.27 \pm 0.03$
	b	$20 \pm 4$	$1043 \pm 23$	$2.0 \pm 0.2$	$0.22 \pm 0.01$

Table 5: Numbers  $N_e$  and  $N_\gamma$  of charged particles ( $e^-$  and  $e^+$ ) and photons passing the top (t) and bottom (b) diamond sensors assuming a pencil-like primary beam. The average particle energies,  $\langle E_e \rangle$  and  $\langle E_\gamma \rangle$ , is given in the right columns. The offsets of the beam are 0, 20 mm and 46 mm.

Offset [mm]	Sensor	$\langle E_{dep}^{tot} \rangle$	$\langle E_{dep}^\gamma \rangle$
		[eV/primary]	
0	t,b	$25.2 \pm 1.5$	$0.74 \pm 0.03$
20	t	$79.9 \pm 4.2$	$1.12 \pm 0.32$
	b	$8.4 \pm 1.8$	$0.60 \pm 0.10$
46	t	$405.0 \pm 18.1$	$2.52 \pm 0.39$
	b	$6.5 \pm 1.8$	$0.53 \pm 0.09$

Table 6: Total deposited energy  $\langle E_{dep}^{tot} \rangle$  and contribution of photons to the energy deposition  $\langle E_{dep}^\gamma \rangle$ . The offsets of the pencil-like beam are 0, 20 mm and 46 mm.

the beam pipe and their energy spectra have not been considered.